4D Printing of Polyethylene Glycol-Grafted Carbon Nanotube-Reinforced Polyvinyl Chloride–Polycaprolactone Composites for Enhanced Shape Recovery and Thermomechanical Performance

Davood Rahmatabadi, Mohammad Amin Yousefi, Shahrooz Shamsolhodaei, Majid Baniassadi, Karen Abrinia, Mahdi Bodaghi, and Mostafa Baghani**

4D printing with carbon nanotube (CNT)-reinforced polymers enables advanced shape-changing materials but faces challenges in CNT dispersion and performance. This study addresses these limitations by functionalizing CNTs with polyethylene glycol (PEG), significantly enhancing dispersion and interfacial bonding within biocompatible polyvinyl chloride (PVC)-polycaprolactone (PCL) composites. The composites, tailored for biomedical applications with a glass transition temperature (T_g) of 37–41 °C, exhibit enhanced mechanical, thermal, and shape-memory properties. At 0.5 wt% CNT, the composite achieves a 25% increase in tensile strength, 95.78% shape fixity, and a 5-s recovery time, offering an optimal balance of strength, flexibility, and rapid shape recovery. Higher CNT concentrations (5 wt%) further improve thermal stability, increasing the decomposition temperature by 20 °C and storage modulus by 670 MPa, although ductility is reduced. PEG grafting prevents CNT agglomeration, enabling high filler loading without compromising printability, as confirmed through uniform nanoparticle dispersion and defect-free fused deposition modeling (FDM)-printed structures. These intelligent composites combine biocompatibility, durability, and excellent shape-memory performance, making them suitable for diverse structural and biomedical applications, such as adaptive medical devices, ergonomic shoe soles, and wearable biosensors. This novel material provides a versatile platform for high-performance, 4D-printed intelligent systems that address current challenges in polymer nanocomposites and advance engineering and biomedical innovations.

1. Introduction

The advent of advanced manufacturing techniques, particularly additive manufacturing (AM), has transformed the production landscape.[1–4] Moving beyond traditional 3D printing, which creates static objects from digital designs, the emergence of 4D printing introduces the dimension of time, enabling objects to change shape in response to external stimuli.[5,6] This innovative approach utilizes smart materials, such as shape-memory polymers (SMPs), that can alter their geometry in response to external stimuli such as water,[7,8] heat,[9,10] light,[11,12] electricity,[13,14] or magnetic fields.[15,16] Recent advancements in programmable materials have enabled precise control over shape transformations, improving applications in biomedical devices,[17–19] soft robotics,[20–22] and adaptive structures including metamaterials.[23–25]

Among the AM techniques, fused filament fabrication (FFF) has been widely recognized as a robust technique for 4D printing due to its versatility and accessibility.[26] FFF, also known as FDM, operates by heating and extruding thermoplastic materials to build 3D structures layer by layer.[27] Thermoplastics are deposited

D. Rahmatabadi, M. A. Yousefi, S. Shamsolhodaei, M. Baniassadi,
K. Abrinia, M. Baghani
School of Mechanical Engineering
College of Engineering
University of Tehran
Tehran 1417614411, Iran
E-mail: baghani@ut.ac.ir

M. Bodaghi
Department of Engineering School of Science and Technology
Nottingham Trent University
Nottingham NG11 8NS, UK
E-mail: mahdi.bodaghi@ntu.ac.uk

The ORCID identification number(s) for the author(s) of this article can be found under https://doi.org/10.1002/aisy.202500113.

DOI: 10.1002/aisy.202500113

through a heated nozzle onto a build plate, creating models with high precision.[28] FDM's precise temperature control enables seamless processing of SMPs, allowing the fabrication of structures that can undergo programmed shape transformations in response to external stimuli. Moreover, the ability to control printing parameters such as layer thickness, infill density, and printing orientation further enhances the tunability of shape-memory effects (SMEs) in 4D-printed structures. This level of control makes FDM particularly advantageous for designing adaptive components with tailored actuation responses. Additionally, its cost-effectiveness and widespread adoption make it a practical choice for developing complex, functional 4D-printed components.[29,30] The choice of materials plays a crucial role in determining the properties of the final product, and polymers have become the most widely utilized material class in the industry due to their versatile behaviour around the T_g. Above T_g, polymers are soft and flexible in their rubbery plateau, whereas below T_g, they exhibit hard and brittle characteristics in their glassy region. Polymers with a T_g above ambient conditions include polyvinyl chloride (PVC), polyethylene terephthalate (PET), and polymethyl methacrylate (PMMA). Conversely, polymers such as low-density polyethylene (LDPE) and silicone exhibit T_g values below room temperature.[31,32]

PVC is one of the most extensively utilized thermoplastic polymers in the industry, valued for its versatility, durability, and cost-effectiveness. Recent studies indicate that PVC is a suitable material for use in 3D printing applications.[33–35] Chemically, PVC is an amorphous thermoplastic polymer produced through the free radical polymerization of vinyl chloride monomer. Although pure PVC exhibits inherent hardness and brittleness, its mechanical properties can be significantly enhanced through the incorporation of plasticizers. The material's excellent chemical resistance, combined with its abrasion and weather resistance, renders it suitable for diverse applications, including pipes and fittings, door and window profiles, flooring, and wire and cable insulation.[36,37] Polycaprolactone (PCL), on the other hand, is a biodegradable polymer widely used in engineering applications, valued for its flexibility, tensile strength, and ease of processability. It demonstrates excellent biocompatibility, supporting cell growth and proliferation, and is compatible with FDM, making it ideal for high-quality 3D printing.[38–41] Furthermore, its ultralow T_g of -60 to $-70\,°C$ and a melting point of 59 to 64 °C in a fully amorphous state and exceptional molecular-level compatibility with PVC enhance its versatility across applications.[35,42] A critical consideration in medical and dental applications is the biocompatibility of polymers that come into contact with the human body. PVC, a durable thermoplastic polymer widely used for its excellent chemical resistance, is inherently bioincompatible. However, blending PVC with biodegradable and biocompatible polymers like PCL, known for its flexibility and tensile strength, can mitigate this limitation. The resulting PVC–PCL composites not only enhance biocompatibility but also achieve a synergy of mechanical properties, offering a versatile solution for applications that require both durability and adaptability across industrial and biomedical fields.[40,43,44]

Research has demonstrated the potential of PVC–PCL composites for advanced applications in 3D and 4D printing. Liu et al.[45] investigated PVC–PCL composites with triple-shape-memory properties and identified PVC–PCL (70/30) as an optimal composition due to its wide glass transition range (0–60 °C) and desirable mechanical characteristics. Sundgren et al.[46] studied the anti-plasticizing effect of PCL on PVC, highlighting the mechanical behaviour of PVC–PCL blends, while our earlier work[47] focused on the biocompatibility of PVC–PCL composites and their environmental advantages over conventional plasticizers. Building on these findings, another of our previous studies,[48] demonstrated that PVC–PCL blends exhibit enhanced shape recovery properties at higher temperatures, with PVC–PCL (90/10) outperforming PVC–PCL (95/5). Notably, PVC–PCL (90/10) achieved a yield stress of 39.71 MPa at room temperature and showed shape recovery stresses of 7.92 and 5.63 MPa at recovery temperatures of 65 and 45 °C, respectively, highlighting its superior performance under higher recovery conditions.

Carbon nanotubes (CNTs) have been widely studied due to their exceptional electrical, thermal, and mechanical properties, which make them a significant focus of research over the past two decades.[49–53] As an example, Ho et al.[54] demonstrated that integrating multiwalled CNTs (MWCNTs) into PCL matrices via 3D printing enhanced scaffolds' mechanical strength, thermal stability, and electrical conductivity. Nanoindentation showed increased elastic modulus and hardness, while biodegradation rates were tunable. These biocompatible PCL–MWCNT composites are promising for cardiac tissue engineering. CNT's unique structure and high aspect ratio, reinforced by carbon-carbon covalent bonds, provide remarkable strength-to-weight ratios, tensile strength of up to 500 GPa, and a low density of $\approx 1.3\ \text{g cm}^{-3}$, making them both stronger and lighter than steel.[55–58] CNTs also exhibit excellent thermal conductivity ($\approx 3500\ \text{Wm}^{-1}\ \text{K}^{-1}$) and stability at high temperatures, along with electrical properties that vary depending on their geometry.[59–61] Despite these advantages, incorporating CNTs into polymer matrices is challenging due to strong van der Waals interactions that lead to agglomeration, which limits their dispersion and negatively impacts composite properties.[62] Grafting polymers onto CNTs has been shown to effectively address these challenges by improving dispersion, enhancing interfacial adhesion, and enabling better load transfer. This process leads to debundling and exfoliation of CNTs, improving solubility and ensuring uniform distribution within the matrix. As a result, polymer-grafted CNT composites exhibit improved mechanical, thermal, and electrical properties, making them suitable for high-performance applications.[49,50,63]

Although CNTs have been widely studied in polymer composites, their effective integration remains a challenge, particularly in achieving uniform dispersion and maintaining processability. Functionalizing CNTs with PEG introduces a crucial improvement in the interaction between the filler and the polymer matrix, which has significant implications for enhancing material properties.[64] Additionally, while MWCNTs offer excellent mechanical and electrical properties, their cytotoxicity and potential biomembrane disruption remain concerns. They can trigger oxidative stress and inflammation due to their high aspect ratio and surface reactivity.[65] PEG grafting mitigates these risks by improving dispersion, reducing aggregation, and forming a biocompatible shield, making PEG-grafted CNTs a safer choice for biomedical and structural applications.[66,67] Furthermore, by enhancing dispersion and interfacial bonding, PEG grafting not only improves biocompatibility but also enables the incorporation of higher CNT loadings without common issues such as agglomeration or reduced processability.[67,68] As CNT content increases, achieving uniform dispersion, maintaining strong filler–matrix interactions, and preventing nozzle clogging in 3D printing become critical challenges. This study is the first to demonstrate that PEG-grafted CNTs simultaneously enhance dispersion, interaction, and printability, enabling high-strength nanocomposites with superior processability at elevated CNT loadings.

In this study, PEG-grafted CNT-reinforced PVC–PCL composites were developed with varying CNT weight percentages (0.5, 2, 3.5, and 5%) to enhance material performance and compatibility. The CNTs were functionalized with polyethylene glycol (PEG) to address the dispersion challenges typically associated with CNTs, thereby ensuring uniform distribution within the polymer matrix and improving interfacial bonding. PEG was specifically chosen for its biocompatibility, hydrophilicity, and ability to stabilize CNTs in polymer systems, offering advantages over other potential modifiers. By overcoming the limitations of conventional CNT integration, this approach enables the fabrication of high-strength, printable nanocomposites with optimized rheology, minimizing processing issues such as increased viscosity and nozzle clogging. The composites were synthesized via melt blending and filament extrusion, followed by 3D printing using FDM. A range of tests, including dynamic mechanical thermal analysis (DMTA), thermogravimetric analysis (TGA), Fourier transform infrared spectroscopy (FTIR), scanning electron microscopy (SEM), mechanical properties (tensile testing and three-point bending), and shape-memory experiments, was performed and demonstrated significant improvements in mechanical, thermal, and structural properties, emphasizing the impact of PEG-grafted CNTs on composite performance. This work addresses a critical gap by presenting a simple and effective method for developing high-performance nanocomposites for 3D printing. Leveraging PEG-grafted CNTs, this approach enhances mechanical properties, particle distribution, and printability, offering significant potential for advanced manufacturing applications requiring material uniformity and high filler content.

2. Experimental Section

2.1. Materials

The primary material used in the preparation of PVC–PCL blends and composites was transparent food-grade PVC granules (K value of 70) sourced from Baspar Plastic Industrial Company, Iran. Polycaprolactone granules were commercially obtained from eSun Co., China. Tetrahydrofuran (THF), a solvent with a boiling point of 66 °C, was obtained from Sigma-Aldrich. THF was employed as a solvent during the modification of oxidized nanoparticles with PEG. Prior to use, it was rigorously dried. PEG with a molecular weight of 400 g mol^{-1} was purchased from Merck, Germany, and utilized for grafting onto CNTs and subsequent chemical modification. CNTs were acquired from US Nano, exhibiting a purity level exceeding 95%. These CNTs possessed an inner diameter of 5–10 nm, an outer diameter of 20–30 nm, and a length of 10–30 micrometers. Sulfuric acid (H_2SO_4) and nitric acid (HNO_3) were obtained from Merck, Germany, with concentrations of 98% and 65%, respectively. Dicyclohexylcarbodiimide (DCC) served as the catalyst for the PEG grafting reaction onto nanoparticles. This coupling agent, appearing as white crystals, was also acquired from Merck, Germany.

2.2. Modification of CNTs

To improve the dispersion and distribution of nanoparticles within the polymer matrix and prevent agglomeration, the surface of the CNTs was functionalized by grafting PEG. CNTs were highly hydrophobic and exhibited poor interaction with polar solvents and polar polymers such as polyethylene oxide (PEO). Grafting PEG onto the surface of CNTs could provide suitable dispersion of nanoparticles in both aqueous and organic solvents.[69,70] Since PEG had a chemical structure very similar to PEO, it was expected to provide good dispersion when attached to the nanoparticle surface. For this purpose, a "grafting to" method was employed, which initially requires the oxidation of CNTs and the creation of carboxylic acid groups on the surface. Subsequently, the oxidized nanoparticles reacted with PEG 400 in the presence of DCC catalyst. The details of the nanoparticle modification process are presented in the following and illustrated in **Figure 1**.

CNTs were oxidized using an acid oxidation method. Acid oxidation was a mild oxidation method that employs a mixture of nitric and sulfuric acids, resulting in the formation of carboxylic acid groups on the nanoparticles. In this method, a mixture of sulfuric acid and nitric acid specifically created carboxylic acid groups on the nanoparticles.[71] The resulting product was called CNT-COOH. Initially, for every 0.4 g of nanoparticles, 100 mL of a mixture of 8 molar sulfuric acid and 8 molar nitric acid was used in a 1:1 volume ratio. The mixture was stirred using a magnetic stirrer at 60 °C for 20 min. Then, this mixture was placed in an ultrasonic bath at 60 °C for 2 h at a power of 60 W and a frequency of 40 kHz. After the completion of the ultrasonic bath, the solution was diluted with distilled water, and the dilution and centrifugation of the mixture were repeated until the pH of the solid nanoparticles reached a neutral range. Finally, the neutralized mixture was dried in an oven under vacuum at 60 °C for 24 h.

2.3. PEG Grafting

A Fischer esterification reaction was used, which involved refluxing alcohol and carboxylic acid in the presence of a catalyst. The reaction was carried out in the presence of a DCC catalyst, in a nonpolar THF solvent, under a nitrogen atmosphere, and for 48 h at 60 °C. This reaction was performed on CNTs oxidized by the acid method. For every 0.5 g of CNTs, 40 mL of dried THF solvent was poured into a flask. Two grams of PEG and 0.05 g of DCC were added to it. The mixture was placed in an ultrasonic bath at 130 W and a frequency of 40 kHz for 15 min. Afterward, the mixture was stirred using a magnetic stirrer at high speed for 48 h under the aforementioned reflux conditions. During this time, a nitrogen gas flow was active. After the reaction time was completed, the functionalized nanoparticles were separated using a 0.45-μm Teflon filter and washed with a sufficient amount of ethanol and distilled water. To ensure the removal of all excess and unreacted PEG, the mixture was centrifuged, and after each centrifugation step, the ethanol solution was removed, and the remaining precipitate in the Falcon tubes was transferred to a new container, and the solvent was added again. In the final step, the precipitate along with the ethanol

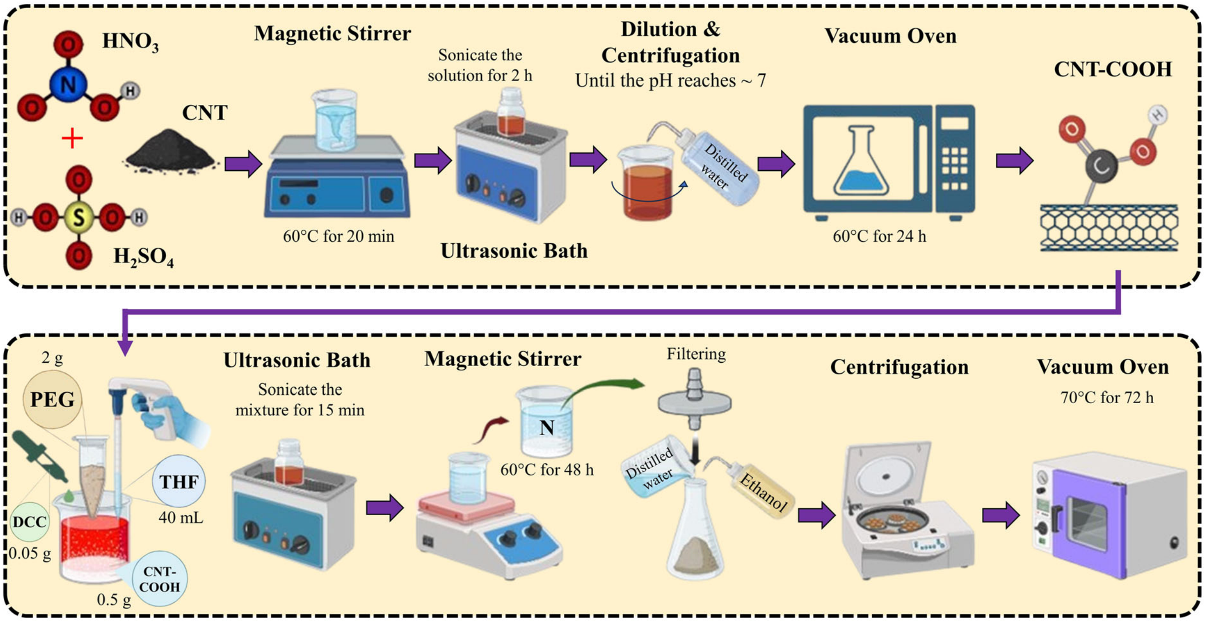

Figure 1. Schematic of the step-by-step process for modifying CNTs via oxidation (CNT-COOH preparation).

solution was kept in a vacuum oven at 70 °C for 72 h, and then the PEG-grafted CNTs were ready for use in composite processing.

2.4. Nanocomposite Preparation

PVC–PCL–CNT composites with varying weight percentages of PEG-grafted CNTs were prepared using the melt mixing method. Prior to mixing, PVC and PCL granules were dried at 80 and 60 °C, respectively, for 24 h to remove moisture. Initially, PVC granules were fed into the internal mixer and completely melted for 2 min at 180 °C and a speed of 100 rpm. PCL granules were then added, followed by the nanoparticles. The mixture was held for 10 min. The output of the internal mixer was a composite in the form of a lump. Subsequently, it was processed into thin sheets with a thickness of less than 1 mm using a hot press. The produced sheets were then granulated. In this way, four composites with weight percentages of 0.5, 2, 3.5, and 5% were prepared (**Table 1**).

Table 1. Compositions of PVC–PCL–CNT blends.

Sample	PVC	PCL	CNT
	[wt%]	[wt%]	[wt%]*
PVC–PCL	90	10	0
PVC–PCL-C0.5	90	10	0.5
PVC–PCL-C2.0	90	10	2.0
PVC–PCL-C3.5	90	10	3.5
PVC–PCL-C5.0	90	10	5.0

*** Note:** CNT content is reported in wt% for consistency but represents phr (parts per hundred rubber) relative to the PVC–PCL blend.

2.5. Filament Production

To print the final samples using FDM, a filament with a diameter of 1.75 mm and a smooth surface was required. This was achieved using a single-screw extruder with a length-to-diameter ratio of 20, a nozzle temperature of 210 °C, and a screw rotation speed of 25 rpm. The same process was repeated for PVC–PCL blends and processed composites at temperatures ranging from 210 to 215 °C.

2.6. 3D Printing

After qualitative and quantitative analysis of the processed filaments, the samples were printed using a custom-built single-nozzle FDM 3D printer. Due to the specific printing conditions of PVC, several critical points were considered for the first time. To ensure the adhesion of the first layer and overcome the poor adhesion of PVC to the printing bed, PVC adhesive was used. The most significant challenge in printing PVC was selecting the appropriate temperature, as the operating temperature range was very limited. In the FDM process, this working range was affected by parameters such as speed, nozzle diameter, and layer thickness, and it significantly impacted the melt rheology, filament buckling, and quality of the final printed part. For this purpose, a constant nozzle printing temperature of 200 °C was considered for all samples. To achieve optimal mechanical properties, the speed, layer thickness, and nozzle diameter were adjusted within the printable range summarized in **Table 2**. It is worth noting that this was the highest possible temperature for printing PVC, and increasing it further caused thermal degradation (becoming yellow in colour). Although printing at lower temperatures (in the range of 170 to 200 °C) was possible under specific printing conditions, reducing the temperature, due to the

Table 2. 3D printing conditions of printed samples.

Printing parameters	PVC–PCL	PVC–PCL–CNT
Velocity (mm/s)	10	10
Temperature (°C)	200	200 - 210
Layer thickness (mm)	0.2	0.2
Nozzle diameter (mm)	0.8	0.8

higher flow rate of PVC and its high melt strength, exacerbated two limitations: nozzle clogging and filament buckling. All samples were printed with 100% infill density and a bed temperature of 60 °C. **Figure 2**a,b demonstrate the processes of nanocomposite preparation and the printed specimens, respectively.

2.7. DMTA

Using ASTM D4065-01, DMTA was performed in a constant temperature range of −50 to 100 °C. The beam-shaped specimen was subjected to a bending state and dimensions of $50 \times 10 \times 1.5\ \text{mm}^3$, and temperature changes and constant frequency were applied at a rate of $5\ °\text{C min}^{-1}$ and 1 Hz, respectively.

2.8. TGA

TGA test was used to compare PVC–PCL with CNT-containing compounds and also to determine the thermal stability of polymer samples. These measurements were performed using a Mettler Toledo TGA/DSC1 device, manufactured in Switzerland. The samples were heated from room temperature to 500 °C at a rate of $10\ °\text{C min}^{-1}$ in a nitrogen atmosphere.

2.9. FTIR

FTIR examined four different samples of CNT with PEG, a pure CNT sample with a repeat of it, and finally a CNT modified with carboxyl functional groups (COOH) in the range of $400–4000\ \text{cm}^{-1}$. It was performed with 14 scans and using a Bruker EQUINOX 55 device.

2.10. Mechanical Properties

Mechanical properties were investigated through tensile and bending tests on various samples. Test specimens for tensile testing and three-point bending were printed with dimensions of $9.5 \times 3.2 \times 3\ \text{mm}^3$ and $50 \times 10 \times 3\ \text{mm}^3$ respectively. The mechanical tests were conducted using three repetitions for each group at a displacement rate of $1\ \text{mm min}^{-1}$, at room temperature, and performed on a Santam testing machine.

2.11. Printability and Morphology

The morphological analysis and evaluation of the printability of the composite's tensile-fractured surface were performed using a Tescan Vega SEM. The samples were first fractured in a brittle manner under liquid nitrogen, following standard laboratory methods. The fractured surfaces were then coated with a thin layer of gold and dried at room temperature. This process facilitated the examination of the bond quality between the PVC–PCL–CNT layers and provided valuable insights into the structural characteristics of the composite.

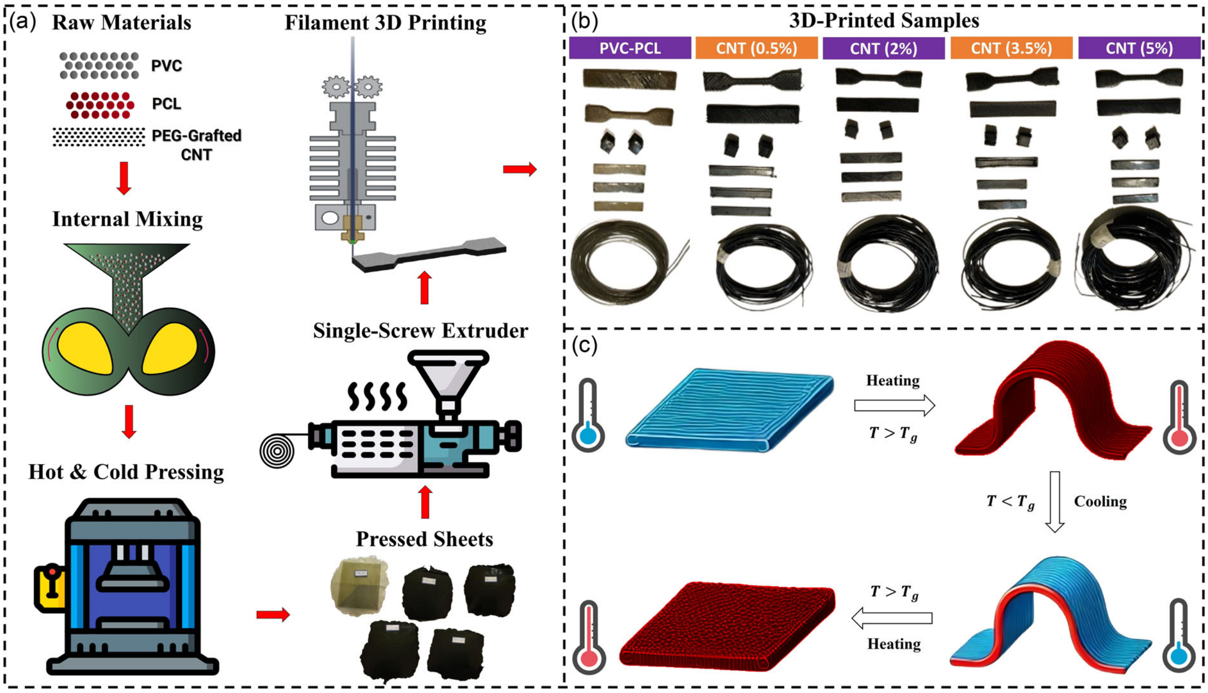

Figure 2. a) Nanocomposite preparation and 3D printing process. b) 3D-printed samples. c) Schematic of the shape recovery process.

2.12. SME

The programming temperatures were determined based on the results of DMTA, which identified three distinct thermal zones: glassy, transition, and rubbery states. The programming and recovery processes were conducted within these zones, enabling the evaluation of SME parameters, including shape fixity (R_f) and shape recovery ratio (R_r). Figure 2c illustrates the shape recovery process.

Beam-shaped samples measuring $50 \times 10 \times 1.5\,\text{mm}^3$ were used for the tests. During the programming stage, the samples were heated in a water bath to 80 °C, a temperature above their glass transition (T_g), and subjected to bending forces to induce deformation. The samples were then cooled to 20 °C in water while maintaining the applied force to stabilize their shape. After cooling, the load was removed. The angle achieved after fixity was recorded as θ_f. The (R_f) was calculated using Equation (1)

$$R_f(\%) = \frac{180 - \theta_f}{180} \times 100 \tag{1}$$

To evaluate shape recovery, the samples were reheated in an 80 °C water bath, where they returned to their original shape as the temperature exceeded T_g and transitioned into the rubbery state. Each recovery test was repeated three times for consistency, and the recovery process was monitored by a video camera to ensure accuracy. The angle achieved after recovery was recorded as θ_r.

The (R_r), were calculated using the Equation (2)

$$R_r(\%) = \frac{\theta_r - \theta_f}{180 - \theta_f} \times 100 \tag{2}$$

3. Results and Discussion

3.1. FTIR

FTIR works on the basis of the absorption of infrared radiation by a material and the specific vibrations of chemical bonds. In fact, each chemical bond in a material, depending on its type and structure, absorbs a specific energy of infrared light, leaving behind a chemical fingerprint, which is essentially a unique spectral pattern.

The results of the FTIR spectrum analysis are shown in **Figure 3**b, with the horizontal axis of the wavelength diagram and the vertical axis of light transmission. By analyzing the peaks of these diagrams in Figure 3b, it is clear that the absorption of certain lights in the range of 3000–3700 cm^{-1}, whose intensity is higher in the COOH sample, is related to the presence of hydroxyl groups (—OH). Also, the light absorption bands at 1500–1800 cm^{-1}, which are clearly observed in the modified CNT, indicate the stretching vibration of the C═O bond. The presence of peaks in the 700–1300 and 2800–3000 cm^{-1} regions also confirms the presence of C—H and C—O—C groups.

Finally, it can be concluded that the surface modification process of CNTs has been successfully carried out and hydroxyl and C═O functional groups have been added to the CNT structure, which indicates an increase in the interaction between nanoparticles and the matrix in composite applications. The presence of the mentioned peaks in the modified sample can also be seen to improve the mechanical and thermal properties of nanomaterials.

3.2. Thermal Properties

As discussed in previous sections, PVC is one of the most widely used polymers because of its good mechanical properties, ease, and economic processability. However, this polymer has a fragile nature, and it is non-biodegradable. Therefore, PCL was incorporated to make it flexible and biocompatible. Besides, CNTs were incorporated to make it obtain more suitable mechanical, electrical, and thermal properties. In this study, the PVC–PCL–CNT composite was characterized using DMTA and TGA in order to research the thermal and mechanical properties of this composite.

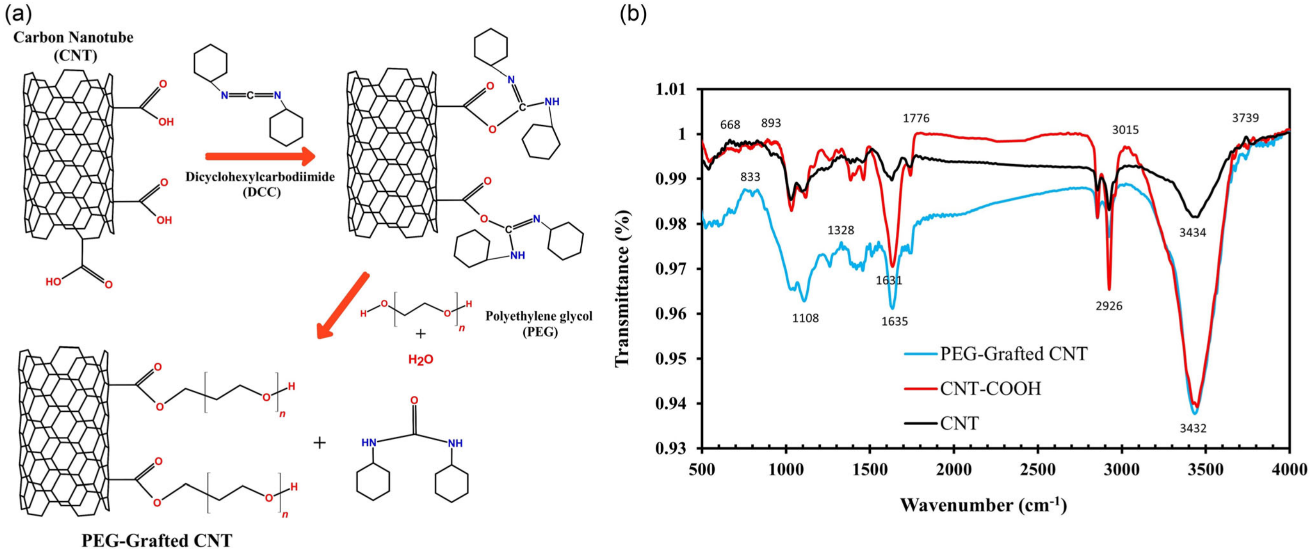

Figure 3. a) Reaction scheme for the functionalization of CNTs with PEG using DCC as a coupling agent. b) FTIR spectra of PEG-grafted CNTs, CNT-COOH, and pristine CNTs.

In DMTA, which is used to analyze the viscoelastic properties of polymers, a small sinusoidal stress is applied to the polymer sample, and its deformation is measured. By analyzing the temperature change or the frequency of the applied stress, information about the storage modulus (E′) and loss coefficient (tan δ) was obtained. The rise of the storage modulus indicates the rise in strength and rigidity of the composite, and the T_g of the polymer can be obtained from the loss coefficient diagram.

Figure 4 presents the thermal analysis results for the PVC–PCL mixture and reinforced nanocomposites with different weight percentages of CNT. As can be seen in Figure 4a,b, which show data of DMTA, the PVC–PCL combination is a completely miscible mixture, a result supported by findings in the literature.[72] The high compatibility of these two thermoplastic polymers has led to this result, and the addition of nanoparticles had no effect on the solubility and morphology of the mixture. The results show that the storage modulus in −50 °C grows with the increase in CNT weight, rising from 2152.78 MPa for the neat PVC–PCL blend to 2592.94 MPa at 0.5 wt% CNT and 2822.9 MPa at 5 wt% CNT. Of course, this increased rate is noticeable compared to the PVC–PCL mixture without nanoparticles. The T_g of the PVC–PCL blend can be identified from the transition region of the storage modulus curve, corresponding to the range of 37–41 °C, which serves as the switching temperature for the shape-memory process. This temperature range aligns closely with human body temperature, making the material suitable for biomedical applications. With the addition of CNTs, the storage modulus slightly increases, particularly at higher CNT contents, due to the restriction of polymer chain mobility caused by the nanoparticles. On the other hand, the reduction of tan δ with the addition of CNTs is noticeable, which indicates the improvement of the elastic behaviour of the material and the reduction of energy loss. This enhancement in modulus and reduced energy dissipation contribute to the improved shape fixity observed in CNT-reinforced composites compared to the neat PVC–PCL blend.

To investigate the thermal properties, TGA and derivative TGA (DTG) were conducted. These tests provide critical insights into the thermal stability, decomposition behaviour, and weight loss processes of materials. Specifically, TGA measures the weight changes of a sample as a function of temperature, while DTG identifies the critical temperatures by analyzing the rate of weight change. The TGA curve illustrates the percentage of weight remaining at various temperatures, while the DTG peaks highlight the temperatures at which weight loss occurs most rapidly.

Figure 4c shows the TGA test results for three materials: pure PVC–PCL, PVC–PCL with 0.5% CNT, and PVC–PCL with 5% CNT. The TGA curves can be divided into three distinct regions. In the first region, up to 100 °C, a slight weight change is observed due to the evaporation of moisture or volatile compounds. In the second region, between 200 and 400 °C, weight loss occurs, but no significant differences are noted among the three materials in this temperature range. In the third region, above 400 °C, the weight loss gradually increases, indicating the complete decomposition of the remaining material structure. The addition of 0.5% CNT does not significantly affect the decomposition temperature, but with 5% CNT, the decomposition temperature of the PVC–PCL blend increases by ≈10–20 °C, demonstrating the thermal stabilization effect of CNTs at higher concentrations.

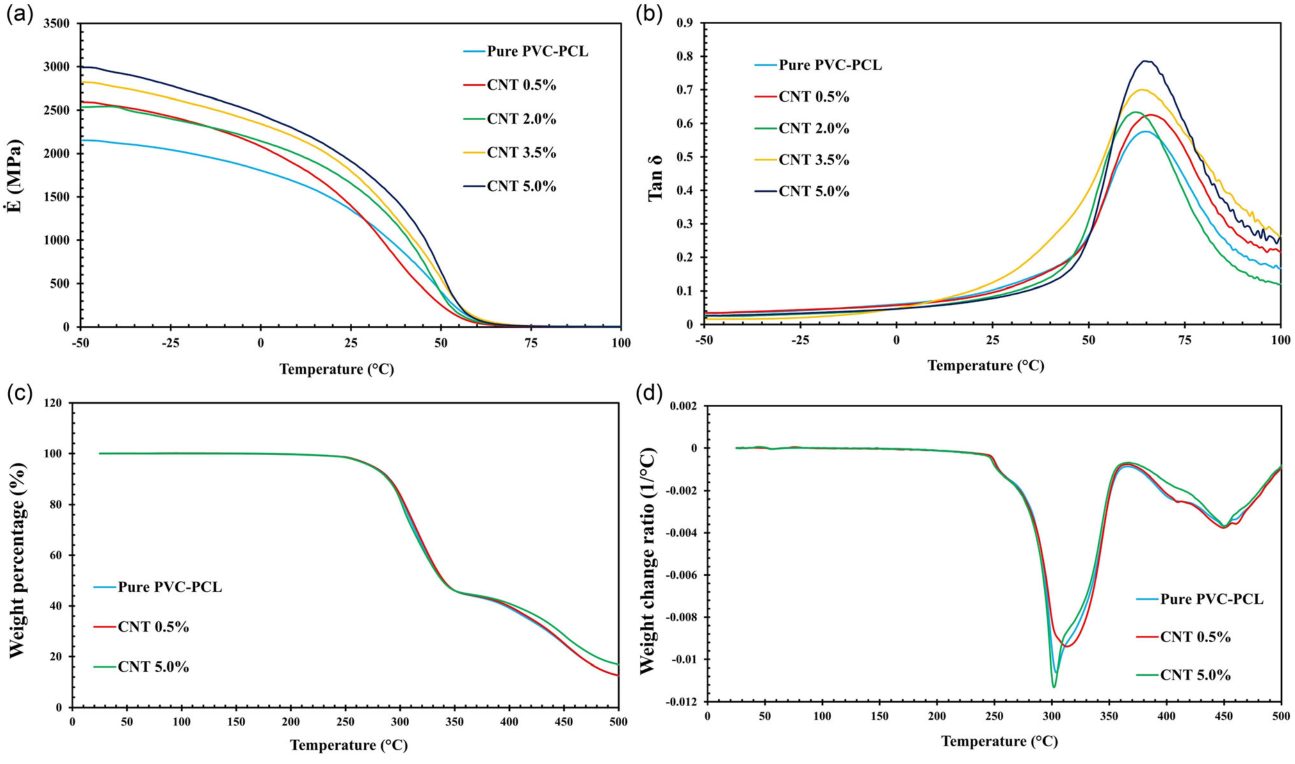

Figure 4. Thermal analysis of PVC–PCL–CNT nanocomposites at varying CNT weight percentages: a) storage modulus, b) Tan δ, c) TGA, and d) DTG.

The DTG results, shown in Figure 4d, reveal two prominent peaks within the temperature ranges of 300–350 and 400–500 °C, corresponding to the critical decomposition temperatures of the materials. The first peak, occurring at ≈310 °C for pure PVC–PCL, shifts to around 315 °C with the addition of 0.5% CNT and remains close to 300 °C for the sample with 5% CNT. At about 310 °C, the height of the peak for the sample with 0.5% CNT is lower than both pure PVC–PCL and the sample with 5% CNT, indicating a reduction in the degradation rate at this temperature. Interestingly, the height of the peak for 5% CNT is slightly higher than that of pure PVC–PCL at this point, suggesting a localized increase in degradation activity. The second peak, observed at ≈445–450 °C for all samples, shows no noticeable difference in peak height among the samples, indicating similar degradation behaviour for the remaining material structure at this stage. These results highlight the nuanced effects of CNT incorporation, with 0.5% CNT contributing to reduced degradation rates during the primary phase, while 5% CNT influences the thermal behaviour differently.

Consequently, the TGA and DTG analyses confirm that the incorporation of CNT nanoparticles into the PVC–PCL blend enhances the thermal stability of the composite materials. The delayed thermal decomposition and reduced degradation rates underscore the stabilizing effect of CNTs, highlighting their potential to improve the performance and reliability of PVC–PCL composites in applications that demand high thermal resistance and structural integrity.

3.3. Mechanical Properties

The mechanical properties of FDM-printed composites were examined under tensile and three-point bending loading modes, considering the effect of CNTs. On the one hand, **Figure 5**a,b depicts quantitative data of the tensile test, including stress–strain diagrams, ultimate tensile strength (UTS), and elongation.

The neat PVC–PCL blend exhibited high elongation and low UTS, reflecting its ductile nature. Adding CNTs significantly increased tensile strength but reduced elongation. At 0.5 wt% CNT, tensile strength improved with minimal loss of ductility, indicating a good balance of strength and toughness due to uniform nanoparticle dispersion. At 2 and 3.5 wt% CNT, tensile strength continued to increase, but elongation dropped sharply, with 2 wt% exhibiting the lowest value, followed closely by 3.5 wt%. This indicates a transition to a stiffer and more brittle behaviour at these CNT concentrations. The 5 wt% CNT composite achieved the strength continued to improve, but elongation showed a slight recovery, possibly due to enhanced load transfer despite the matrix's stiffness.

Therefore, the bar chart in Figure 5b quantitatively highlights these trends. Tensile strength increased steadily with higher CNT content, peaking at 5 wt%, while elongation showed a nonlinear trend. The highest elongation occurred at pure PVC–PCL, followed by a sharp decline at 2 and 3.5 wt% CNT. This demonstrates a clear trade-off between strength and ductility: lower

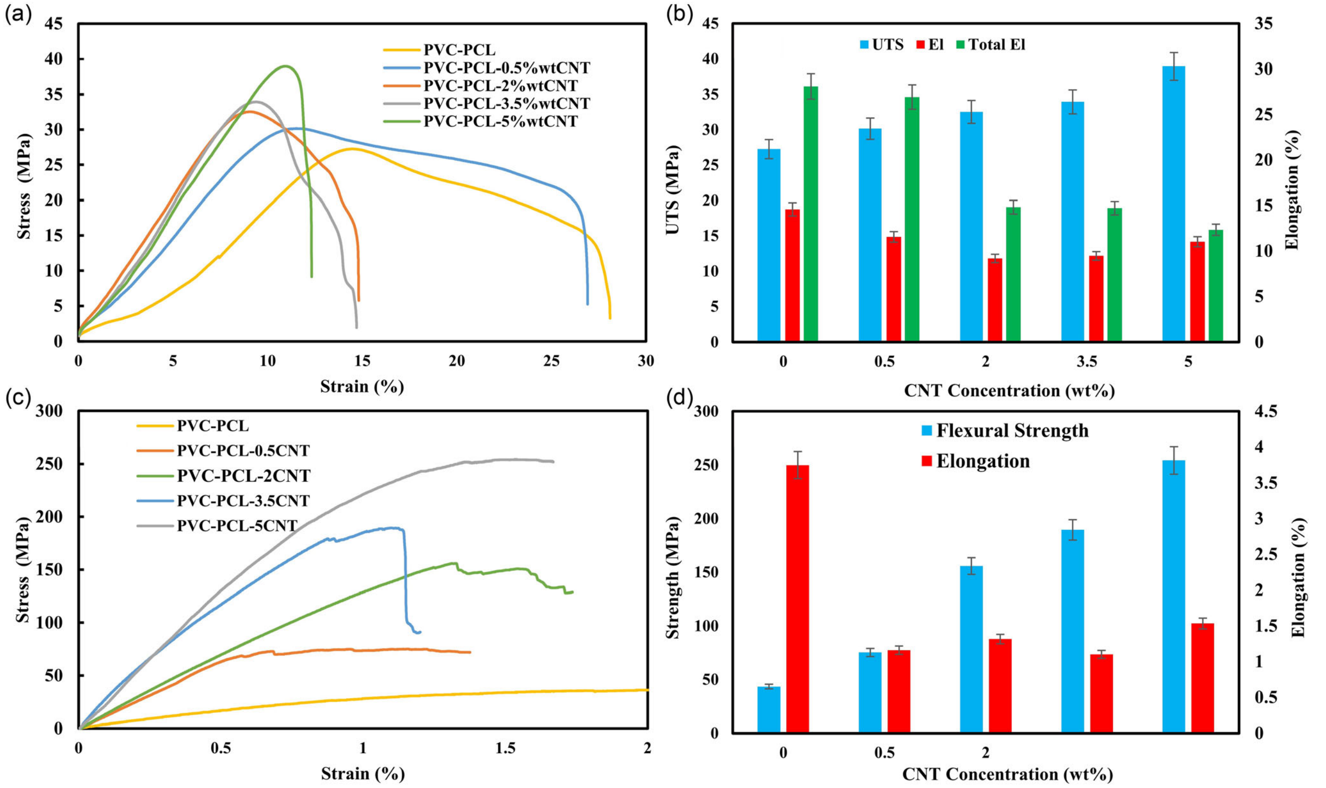

Figure 5. Mechanical test results based on the weight percentage of CNT nanoparticles in PVC–PCL blends: a) stress–strain diagrams from tensile tests, b) quantitative results of UTS and elongation, c) stress–strain diagrams from three-point bending tests, and d) quantitative results of flexural strength and elongation.

CNT concentrations promote toughness, while higher concentrations favor rigidity.

The reinforcing effect of CNTs can be attributed to their ability to transfer stress effectively within the matrix. Surface modification, such as PEG grafting, ensures uniform dispersion and minimizes agglomeration. Figure 3a illustrates how PEG grafting enhances CNT dispersion and interfacial bonding. By reducing van der Waals interactions, PEG prevents CNT agglomeration, which otherwise leads to stress concentration points and premature failure. Additionally, the presence of oxidized functional groups on CNTs facilitates hydrogen bonding, further strengthening the polymer network. This improved dispersion and interaction enhance load transfer, resulting in increased tensile and flexural strength while also improving printability by reducing viscosity fluctuations and preventing nozzle clogging. However, at higher CNT loadings, the FDM process introduces challenges like microvoids and reduced interlayer adhesion, contributing to brittleness. In immiscible polymer systems, failure typically initiates with the development of microcracks in the weaker phase or at the interface between components.[73,74] These regions serve as stress concentration points, significantly contributing to the initiation of the failure process.[75] Conversely, the formation of a miscible compound with strong molecular-level bonding, as seen in miscible PVC–PCL systems, enhances mechanical properties by reducing stress concentration and improving structural integrity.[43]

In conclusion, 0.5 wt% CNT provides an optimal balance of strength and ductility, making it suitable for flexible and tough applications. Higher CNT contents (3.5–5 wt%) are ideal for applications requiring superior strength and rigidity.

On the other hand, Figure 5c,d depicts the results of the three-point bending tests, including flexural strength and deformation behaviour under bending loads. In general, the flexural strength increases with higher CNT content, aligning with the trends observed in the tensile tests. The neat PVC–PCL blend shows the lowest flexural strength due to its ductile nature, while CNT-reinforced composites exhibit improved strength, indicating the reinforcing effect of the CNTs.

However, the elongation behaviour under bending is irregular. The 3.5% CNT sample shows a sudden and brittle failure, which could be attributed to the uneven distribution of nanoparticles and the formation of microvoids during the printing process. This irregularity in elongation trends may also be influenced by factors such as print quality and the consistency of nanoparticle dispersion within the matrix. These observations suggest that while CNTs enhance the flexural strength, challenges such as agglomeration, microvoids, and printing defects can impact the overall mechanical performance, particularly at higher CNT concentrations. These results demonstrate the potential of PVC–PCL–CNT composites for a wide range of structural and flexible applications, with insights into optimizing CNT content and FDM parameters for improved performance. The next section further examines these issues, focusing on print quality and nanoparticle distribution.

3.4. Printability and Morphology

Figure 6 demonstrates cross-sectional images of FDM-printed nanocomposites after brittle failure in liquid nitrogen, along with SEM images of filaments for each CNT percentage. As can be observed, considering the number of microvoids and interlayer adhesion, the print quality of all four nanocomposites is acceptable and satisfactory. The presence of microvoids in the FDM process is inevitable and represents a fundamental challenge of this method. It is highly dependent on feed rate and system, cooling speed of layers, and raster shrinkage. These factors are influenced by a combination of printing parameters, part geometry, and the intrinsic properties of the printing material. The feed rate and system are the most critical and challenging parameters, while all three aspects are interconnected. Material properties, such as rheology and melt strength, play a key role and can be adjusted through printing parameters like temperature, speed, nozzle diameter, and layer thickness. Higher temperatures can lead to better filament melting and improved interlayer adhesion, enhancing feed rate. However, in some cases, higher temperatures may also increase raster shrinkage and exacerbate the presence of microvoids.[76–80]

For semicrystalline thermoplastics, higher printing temperatures are recommended to achieve full crystal melting. In temperature-sensitive materials like PVC, with a limited operational temperature range, excessive temperature increases are not feasible. For composites containing nanoparticles, higher temperatures are suggested to prevent nozzle clogging. However, for PVC–PCL blends, this is not possible, and the samples were printed at 200 °C. Low temperatures can cause issues related to poor fluidity (high viscosity) and increase the likelihood of buckling during printing. To mitigate this, using a larger layer thickness to enhance the feed rate is recommended.

For printing the nanocomposites, a nozzle diameter of 0.8 mm was used. As shown in Figure 6d, the composite containing 5 wt% CNTs exhibited satisfactory print quality similar to the other three composites, primarily due to the proper distribution of nanoparticles. The use of composites with nanoparticles often faces challenges like nozzle clogging due to improper dispersion and agglomeration of particles. In this study, for the first time, modified CNTs functionalized with PEG grafting were used, which contributed to achieving an improved nanoparticle distribution in the PVC–PCL matrix for all four printed composites, as presented in Figure 6e–h. These images confirm that the PVC–PCL blend is compatible, and the addition of nanoparticles does not alter the compatibility or miscibility of the base polymer. This result has previously been examined and confirmed through DMTA thermal analysis. The available literature indicates that polyesters such as PCL and chlorinated polymers like PVC exhibit favorable intermolecular interactions and closely aligned solubility parameters, leading to some level of miscibility.[81–83] Based on these images, the addition of 0.5 wt% CNTs results in a highly dispersed and nearly uniform distribution within the matrix. This uniform distribution is maintained even with the increase in nanoparticle content to 3.5 and 5 wt%.

As shown in Figure 6d, the composite containing 5 wt% CNT exhibits no uneven distribution or particle agglomeration. This achievement is largely attributed to the surface modification of nanoparticles with PEG, which enhances compatibility between the CNTs and the polymer matrix. The PEG grafting reduces the van der Waals interactions among CNTs, preventing their agglomeration and promoting better dispersion within the matrix. Additionally, PEG acts as an effective interface, improving the interaction between the hydrophobic CNTs and the hydrophilic components of the PVC–PCL matrix. By improving wettability and reducing interfacial tension, PEG grafting facilitates the

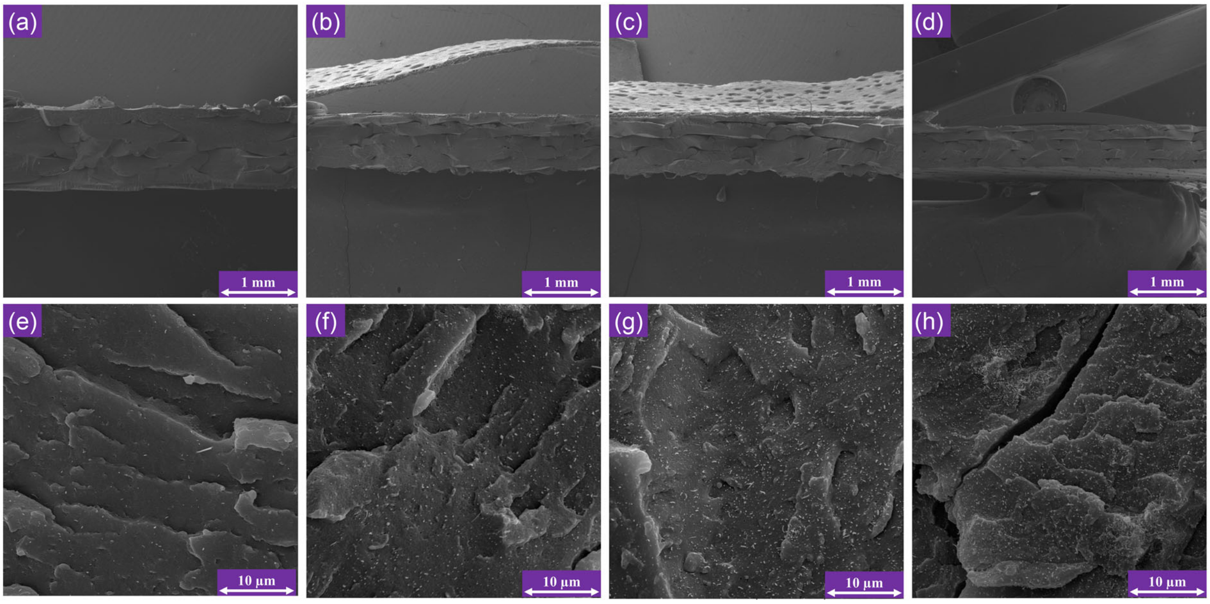

Figure 6. SEM images of filaments at varying CNT percentages a–d) and the corresponding distribution of modified nanoparticles in the PVC–PCL matrix e–h): (a,e) 0.5 wt% CNT, (b,f) 2.0 wt% CNT, (c,g) 3.5 wt% CNT, and (d,h) 5.0 wt% CNT.

integration of CNTs into the polymer blend without disrupting the miscibility or morphology of the base materials. This well-distributed nanoparticle incorporation significantly contributes to the mechanical uniformity and printability observed in the composites.

Moreover, PEG grafting not only improves nanoparticle dispersion but also enhances processing stability during printing by minimizing variations in viscosity. This ensures consistent material flow and layer deposition, resulting in composites with superior structural integrity and fewer defects. Previous studies have shown that optimizing processing conditions plays a key role in controlling surface morphology and improving interlayer adhesion in 3D-printed composites.[84–86] The improved interfacial bonding between CNTs and the matrix enhances load-bearing capacity, reducing microcrack initiation and improving material durability. The uniform CNT distribution facilitates more effective stress transfer, resulting in increased tensile strength and toughness. Continuous improvements in mechanical properties, along with the relative preservation of ductility and consistent, high-quality printability, are direct results of the appropriate nanoparticle distribution facilitated by PEG grafting. Additionally, the electrical performance of these nanocomposites benefits from PEG-assisted dispersion. The well-distributed CNTs establish an interconnected conductive network at lower filler concentrations, allowing for enhanced charge transport. This ensures improved conductivity without requiring excessive CNT loading, which could otherwise compromise mechanical flexibility and processability. Strategies such as fine-tuning processing temperatures, reducing microvoids, and ensuring layer adhesion may further enhance the overall integrity and performance of the composites.

3.5. SME

The shape-memory behaviour of PVC–PCL–CNT composites was evaluated through shape fixity and shape recovery, calculated using Equation (1) and (2). The DMTA provides critical insights into the storage modulus and glass transition temperature of the composites, both of which play a key role in the observed SME during thermal activation.

The T_g of the PVC–PCL matrix, which is ≈37–41 °C, serves as the switching temperature for the shape-memory process, aligning closely with the range of body temperature. When the composites are heated above T_g, the material transitions from the glassy state to the rubbery state, becoming flexible and allowing it to be programmed into a temporary shape. Upon cooling, the material retains this deformed shape due to its higher modulus in the glassy state, which contributes to the observed shape fixity. The DMTA results further reveal that the incorporation of CNTs slightly increases the storage modulus, particularly at higher CNT contents, due to their reinforcing effect. This increase in modulus stabilizes the deformed shape and explains the improved shape fixity values observed in CNT-reinforced composites compared to the neat PVC–PCL blend.

The results for shape fixity demonstrate a significant improvement with the addition of CNTs. The pure PVC–PCL sample exhibited a shape fixity of 82.35%, while the composite containing 0.5 wt% CNT achieved the highest value of 95.78%. This improvement can be attributed to the reinforcing effect of CNTs, which restrict polymer chain mobility, thereby stabilizing the deformed shape. However, for composites with 2.0, 3.5, and 5.0 wt% CNT, shape fixity values slightly decreased to 91.21, 89.75, and 90.00%, respectively. This reduction indicates a minor trade-off between fixity and material stiffness at higher CNT loadings, where increased stiffness may limit the material's ability to hold the programmed shape as effectively.

During the shape recovery process, reheating the samples above T_g allows the material to transition back into its rubbery state, enabling recovery to the original shape. The shape recovery performance of the composites was analyzed over time, as shown in **Figure 7**. According to this figure, nearly 100% shape recovery is achieved in all samples; however, the composites with varying CNT contents exhibit different recovery times. The pure PVC–PCL sample demonstrated the slowest recovery, requiring ≈8–10 s to achieve more than 95% recovery, which is attributed to the absence of reinforcement and slower thermal response. By incorporating CNTs, the recovery rate improved significantly. The composite with 0.5 wt% CNT exhibited the fastest recovery, achieving more than 95% recovery within 5 s due to the uniform dispersion of CNTs, which enhance heat transfer and stress recovery.

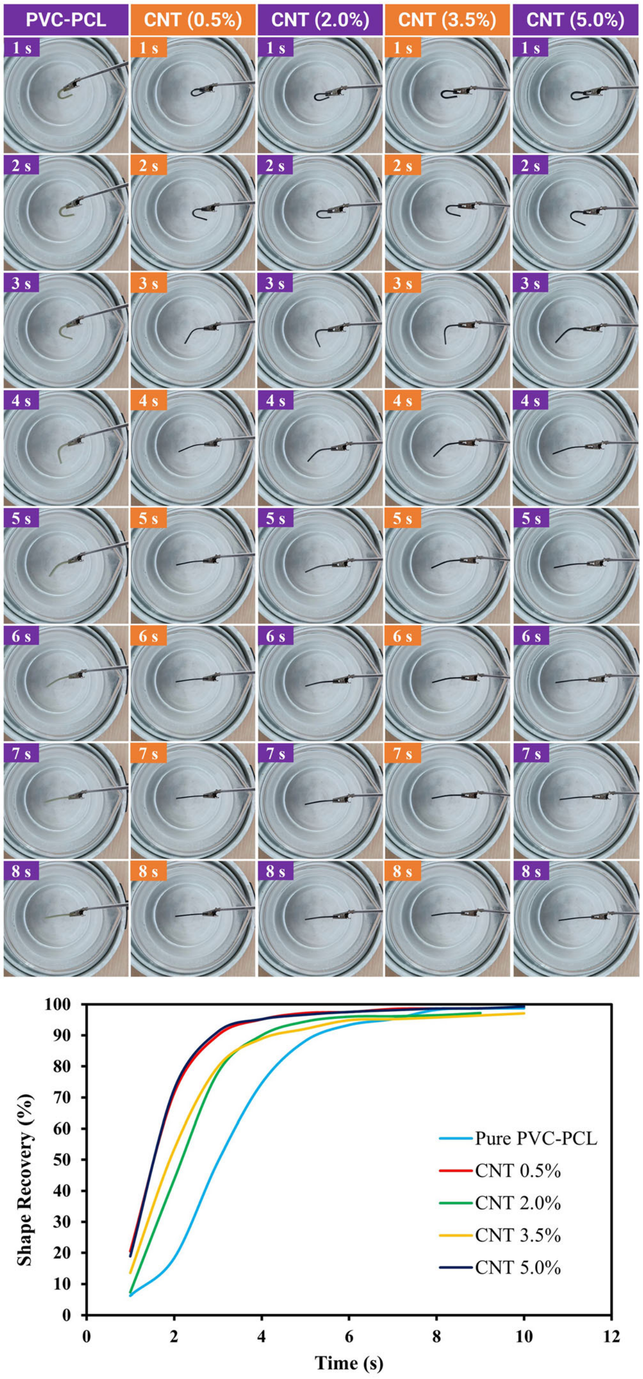

Figure 7. Shape recovery (%) in terms of time in a water bath.

For the 2.0 wt% CNT composite, the shape recovery exceeded 95% within 7 s, indicating a significant improvement compared to the pure blend, though slightly slower than the 0.5 wt% CNT composite due to increased stiffness. Similarly, the 3.5 wt% CNT composite achieved more than 95% recovery in 8 s, demonstrating effective recovery despite the increased rigidity of the matrix. The 5 wt% CNT composite displayed a slightly faster recovery compared to the 3.5 wt% sample, achieving 95% recovery within ≈7 s, reflecting a balance between stiffness and thermal response at this concentration.

Overall, the addition of CNTs significantly enhances both shape fixity and shape recovery performance. The optimal performance was observed at 0.5 wt% CNT, achieving the highest fixity and the fastest recovery time. Composites with higher CNT loadings (2.0, 3.5, and 5.0 wt%) maintained excellent recovery but exhibited slight delays in achieving more than 95% recovery due to increased material stiffness. These results confirm the critical role of CNTs in enhancing the shape-memory behaviour of PVC–PCL composites, making them suitable for applications requiring rapid and reliable shape recovery. A key advantage of this SMP is its superior SME compared to commercial materials such as PLA, PETG, and PU-based SMPs.[47,87,88]

4. Potential Applications

The PVC–PCL–CNT composite exhibits a unique combination of properties, including biocompatibility, energy absorption, high thermal resistance, and mechanical flexibility, which make it highly suitable for various practical applications. This material demonstrates excellent performance in areas such as hand and leg splints,[30,89] shoe soles,[90,91] and biosensors[92,93] due to its ability to integrate structural functionality with adaptability and durability.[94] **Figure 8** illustrates a schematic of potential applications for this novel composite.

For hand and leg splints, the PVC–PCL–CNT composite provides significant advantages. Its biocompatibility ensures safety for direct contact with the body, while its shape-memory properties enable it to be reshaped and programmed to recover at temperatures of 37–41 °C, aligning with the human body's natural temperature range. Unlike traditional splints, which often loosen over time due to prolonged use or changes in swelling, this composite allows for controlled hardening whenever needed by applying heat. This feature enables the splint to be reheated and molded tightly around the affected limb, providing a snug and secure fit while effectively stabilizing the bone. Additionally, the material's energy absorption properties reduce impact-related stress, enhancing both comfort and functionality for the user during recovery. Its high thermal resistance further ensures stability and reliability under demanding conditions, expanding its usability beyond typical environments.

The composite is also well-suited for use in shoe soles due to its combination of softness and resilience. The miscibility of PVC and PCL ensures a uniform structure with excellent energy absorption, making it ideal for ergonomic footwear. Under moderate heating, the composite can adapt to the user's foot shape,

Figure 8. Schematic of potential applications for PVC–PCL–CNST composite.

creating a customized fit that improves comfort during prolonged use. The high thermal stability provided by CNTs enhances durability under extreme conditions, ensuring durability under repeated stress, making it especially advantageous for sports or therapeutic footwear applications.

In biosensors, the PVC–PCL–CNT composite offers unique capabilities due to the electrical conductivity introduced by CNTs. This feature, combined with the material's flexibility and biocompatibility, makes it an excellent candidate for the development of wearable biosensors for health monitoring. The thermal stability and mechanical robustness of the composite ensure reliable performance, while its adaptability allows it to conform to the surface of human skin, improving signal accuracy. These properties make it suitable for a wide range of biosensing applications, including wearable devices and diagnostic tools.

In summary, the PVC–PCL–CNT composite's exceptional properties enable it to address challenges in medical, ergonomic, and technological fields. Its combination of biocompatibility, thermal adaptability, and durability highlights its potential for practical applications, making it a valuable material for advanced engineering solutions.

5. Conclusion

In this study, PVC–PCL–CNT nanocomposites with four different weight percentages of modified CNT nanoparticles were developed and evaluated for their mechanical properties and shape-memory performance. This research represents a novel approach to enhancing polymer composites through PEG-grafted CNT reinforcement. The key findings are as follows: 1) the addition of CNTs increased the storage modulus by 31% (from 2152.78 MPa for the neat PVC–PCL to 2822.9 MPa at 5 wt% CNT), reflecting enhanced rigidity and reduced polymer chain mobility. The glass transition temperature was maintained within the range of 37–41 °C, aligning with human body temperature and making the material highly suitable for biomedical applications. Thermal stability improved significantly, with the decomposition temperature increasing by up to 20 °C at 5 wt% CNT. 2) Tensile and bending tests revealed that 0.5 wt% CNT achieved a 25% increase in tensile strength with minimal loss of ductility, offering the best balance of strength and elongation. Higher CNT contents, such as 5 wt%, achieved the highest flexural strength, but with reduced ductility and increased brittleness, making them better suited for rigid applications. 3) Morphological evaluation indicated a uniform distribution of CNTs across the matrix, ensuring consistent mechanical properties and minimizing defects such as agglomeration. This distribution also improved interlayer adhesion and minimized microvoids, enabling reliable FDM processing even at higher CNT concentrations, which is often challenging for nanoparticle-reinforced composites. 4) CNT reinforcement enhanced shape fixity and recovery performance. The composite with 0.5 wt% CNT exhibited the highest shape fixity (95.78%) and the fastest recovery time (5 s), confirming its suitability for adaptive applications requiring rapid and reliable recovery.

Additionally, this study achieved several key milestones: 1) successful surface modification of CNTs using oxidation and PEG grafting, which improved compatibility and dispersion within the matrix, addressing a critical challenge in polymer-nanoparticle composites; 2) achieving uniform CNT dispersion within the matrix, ensuring defect-free, high-quality filament production and enabling reliable, consistent 3D printing, even at elevated CNT loadings; 3) demonstrating superior mechanical properties that surpass standard materials used in FDM for CNT-reinforced composites, with better elongation compared to commercial filaments available in the market; and 4) demonstrating desirable shape-memory behaviour with activation capability within the human body temperature range (37–41 °C), reinforcing the biocompatibility of the composite for biomedical applications such as splints and adaptive medical devices.

These findings collectively highlight the potential of PVC–PCL–CNT composites for applications requiring adaptability, thermal stability, biocompatibility, and improved mechanical performance in both structural and biomedical fields. Further exploration of indirect stimulation capabilities remains a promising avenue for future research.

Conflict of Interest

The authors declare no conflict of interest.

Author Contributions

Davood Rahmatabadi: conceptualization (lead); data curation (lead); formal analysis (lead); investigation (lead); methodology (lead); validation (lead); writing—original draft (lead); writing—review editing (lead). **Mohammad Amin Yousefi**: data curation (supporting); investigation (supporting); methodology (supporting); validation (supporting); writing—review editing (supporting). **Shahrooz Shamsolhodaei**: data curation (supporting; formal analysis (supporting); investigation (supporting); methodology (supporting); writing—review & editing (supporting). **Majid Baniassadi**: investigation (supporting); methodology (supporting); supervision (supporting); writing—review editing (supporting). **Karen Abrinia**: investigation (supporting); methodology (supporting); supervision (supporting); writing—review editing (supporting). **Mahdi Bodaghi**: conceptualization (equal); investigation (lead); methodology (equal); supervision (equal); validation (supporting); writing—review editing (lead). **Mostafa Baghani**: formal analysis (equal); investigation (equal); methodology (equal); supervision (lead); writing—review editing (equal).

Data Availability Statement

The data that support the findings of this study are available from the corresponding author upon reasonable request.

Keywords

3D/4D printing, biocompatible composites, fused deposition modeling, material extrusions, polyethylene glycol-grafted carbon nanotubes, polyvinyl chloride–polycaprolactones

Received: January 25, 2025
Revised: March 18, 2025
Published online:

---

[1] M. B. Khan, K. Schäfer, F. Hofmann, M. Lutzi, E. S. Oliveros-Mata, O. Pylypovskyi, D. Makarov, O. Gutfleisch, *Adv. Intell. Syst.* **2024**, 2400620.

[2] A. Hassan, T. Alomayri, M. F. Noaman, C. Zhang, *Arch. Comput. Methods Eng.* **2025**, 1.

[3] X. Zuo, Y. Zhou, K. Hao, C. Liu, R. Yu, A. Huang, C. Wu, Y. Yang, *Adv. Sci.* **2024**, *11*, 2306360.

[4] S. Chen, S. B. Khan, N. Li, C. Xiao, *J. Manuf. Process.* **2025**, *133*, 576.

[5] K. Chachlioutaki, N. Papas, Z. Chatzis, O. L. Katsamenis, S. K. Robinson, K. Tsongas, N. Bouropoulos, D. G. Fatouros, D. Tzetzis, C. Karavasili, *Adv. Intell. Syst.* **2024**, 2400526.

[6] D. Rahmatabadi, K. Mirasadi, A. Bayati, M. Khajepour, M. Baniassadi, K. Abrinia, M. Baghani, I. Ghasemi, M. Bodaghi, *Appl. Mater. Today* **2024**, *40*, 102361.

[7] C. Shuai, Z. Wang, S. Peng, Y. Shuai, Y. Chen, D. Zeng, P. Feng, *Mater. Chem. Front.* **2022**, *6*, 1456.

[8] D. Schönfeld, S. Koss, N. Vohl, F. Friess, D. Drescher, T. Pretsch, *Materials* **2023**, *16*, 3094.

[9] D. Rahmatabadi, A. Bayati, M. Khajepour, K. Mirasadi, *Mater. Chem. Phys.* **2024**, *325*, 129737.

[10] D. Rahmatabadi, I. Ghasemi, M. Baniassadi, K. Abrinia, M. Baghani, *J. Mater. Sci.* **2023**, *58*, 7227.

[11] C. Lin, X. Xin, L. Tian, D. Zhang, L. Liu, Y. Liu, J. Leng, *Compos. Part B Eng.* **2024**, *274*, 111257.

[12] S. Miao, Y. Xing, X. Li, B. Sun, Z. Du, H. Cao, P. Guo, Y. Chang, Y. Tian, M. Yao, K. Chen, D. Xiao, X. Zhang, B. Zhao, K. Pan, J. Sun, X. Liang, *Appl. Mater. Today* **2024**, *40*, 102412.

[13] H. Zhang, S. Huang, J. Sheng, C. Wang, J. Zhang, M. Zhu, E. Agyenim-Boateng, C. Liang, B. Xue, H. Yang, J. Zhou, J. Lu, *Addit. Manuf.* **2023**, *78*, 103836.

[14] F. Jin, F. Wang, P. Guo, M. Lyu, L. Wang, D. Gao, L. Sang, *Chem. Eng. J.* **2025**, *508*, 160450.

[15] M. A. Yousefi, D. Rahmatabadi, M. Baniassadi, M. Bodaghi, M. Baghani, *Macromol. Rapid Commun.* **2024**, *46*, 2400661.

[16] K. Mirasadi, D. Rahmatabadi, I. Ghasemi, M. Khodaei, M. Baniassadi, M. Bodaghi, M. Baghani, *Polymers* **2024**, *16*, 1398.

[17] M. Ramezani, Z. Mohd Ripin, *J. Funct. Biomater.* **2023**, *14*, 347.

[18] R. Das, T. L. Cabaniss, S. A. Pineda-Castillo, B. N. Bohnstedt, Y. Liu, C.-H. Lee, *J. Mech. Behav. Biomed. Mater.* **2024**, *160*, 106784.

[19] M. Yang, Y. Xu, X. Xin, C. Zeng, Y. Li, C. Lin, Y. Liu, Y. Guo, J. Leng, *Adv. Funct. Mater.* **2025**, 2412533.

[20] M. López-Valdeolivas, D. Liu, D. J. Broer, C. Sánchez-Somolinos, *Macromol. Rapid Commun.* **2018**, *39*, 1700710.

[21] S. Y. Hann, H. Cui, M. Nowicki, L. G. Zhang, *Addit. Manuf.* **2020**, *36*, 101567.

[22] H. M. Pan, J. Sarkar, A. Goto, *ACS Appl. Polym. Mater.* **2022**, *4*, 8676.

[23] T. van Manen, S. Janbaz, K. M. B. Jansen, A. A. Zadpoor, *Commun. Mater.* **2021**, *2*, 56.

[24] X. Zhou, L. Ren, Z. Song, G. Li, J. Zhang, B. Li, Q. Wu, W. Li, L. Ren, Q. Liu, *Compos. Part B Eng.* **2023**, *254*, 110585.

[25] F. Wenz, D. Schönfeld, S. C. L. Fischer, T. Pretsch, C. Eberl, *Adv. Eng. Mater.* **2023**, *25*, 2201022.

[26] M. Bodaghi, L. Wang, F. Zhang, Y. Liu, J. Leng, R. Xing, M. D. Dickey, S. Vanaei, M. Elahinia, S. Zaman, H. Soleimanzadeh, T. Bar, *Smart Mater. Struct.* **2024**, *33*, https://doi.org/10.1088/1361-665X/ad5c22.

[27] D. S. Xu, Z. Q. Su, B. Lalit, Y. Qin, *Meas. Sci. Technol.* **2022**, *33*, 065106.

[28] F. Qian, R. Jia, M. Cheng, A. Chaudhary, S. Melhi, S. D. Mekkey, N. Zhu, C. Wang, F. Razak, X. Xu, C. Yan, X. Bao, Q. Jiang, J. Wang, M. Hu, *Adv. Compos. Hybrid Mater.* **2024**, *7*, 1.

[29] S. Valvez, P. N. B. Reis, L. Susmel, F. Berto, *Polymers* **2021**, *13*, 701.

[30] C.-Y. Y. Cheng, H. Xie, Z.Y. Xu, L. Li, M.-N. N. Jiang, L. Tang, K.-K. K. Yang, Y.-Z. Z. Wang, *Chem. Eng. J.* **2020**, *396*, 125242.

[31] T. Makki, S. H. Vattathurvalappil, R. Theravalappil, A. Nazir, A. Alhajeri, M. A. Azeem, E. Mahdi, A. C. Ummer, U. Ali, *Compos. Part C Open Access* **2024**, *14*, 100472.

[32] A. Karimi, D. Rahmatabadi, M. Baghani, *Polymers* **2024**, *16*, 831.

[33] I. Calafel, R. H. Aguirresarobe, M. I. Peñas, A. Santamaria, M. Tierno, J. I. Conde, B. Pascual, *Materials* **2020**, *13*, 178.

[34] M. I. Peñas, M. I. Calafel, R. H. Aguirresarobe, M. Tierno, J. I. Conde, B. Pascual, A. Santamaría, *Polymers* **2020**, *12*, 2070.

[35] M. E. Pekdemir, E. Öner, M. Kök, I. N. Qader, *Iran. Polym. J.* **2021**, *30*, 633.

[36] C. Mijangos, I. Calafel, A. Santamaría, *Polymer* **2023**, *266*, 125610.

[37] P. Lieberzeit, D. Bekchanov, M. Mukhamediev, *Polym. Adv. Technol.* **2022**, *33*, 1809.

[38] F. Liu, C. Vyas, G. Poologasundarampillai, I. Pape, S. Hinduja, W. Mirihanage, P. Bartolo, *Macromol. Mater. Eng.* **2018**, *303*, 1700494.

[39] M. Gharibshahian, M. Salehi, N. Beheshtizadeh, M. Kamalabadi-Farahani, A. Atashi, M.-S. Nourbakhsh, M. Alizadeh, *Front. Bioeng. Biotechnol.* **2023**, *11*, 1168504.

[40] Z. U. Arif, M. Y. Khalid, R. Noroozi, A. Sadeghianmaryan, M. Jalalvand, M. Hossain, *Int. J. Biol. Macromol.* **2022**, *218*, 930.

[41] C. T. Roberts, S. K. Beck, C. M. Prejean, L. M. Graul, D. J. Maitland, M. A. Grunlan, *J. Mater. Chem. B* **2024**, *12*, 3694.

[42] Y. Xu, Y. Xiong, S. Guo, *J. Appl. Polym. Sci.* **2020**, *137*, 48803.

[43] D. Rahmatabadi, M. Aberoumand, K. Soltanmohammadi, E. Soleyman, I. Ghasemi, M. Baniassadi, K. Abrinia, M. Bodaghi, M. Baghani, *Macromol. Mater. Eng.* **2023**, *308*, 2300114.

[44] M. E. Pekdemir, *Fibers Polym.* **2021**, *22*, 2861.

[45] W. Liu, R. Zhang, M. Huang, X. Dong, W. Xu, N. Ray, J. Zhu, *Polymer* **2016**, *104*, 115.

[46] N. Sundgren, G. Bergman, Y. J. Shur, *J. Appl. Polym. Sci.* **1978**, *22*, 1255.

[47] M. Aberoumand, K. Soltanmohammadi, D. Rahmatabadi, E. Soleyman, I. Ghasemi, M. Baniassadi, K. Abrinia, M. Bodaghi, M. Baghani, *Macromol. Mater. Eng.* **2023**, *308*, 2200677.

[48] D. Rahmatabadi, M. Aberoumand, K. Soltanmohammadi, E. Soleyman, I. Ghasemi, M. Baniassadi, K. Abrinia, M. Bodaghi, M. Baghani, *Adv. Eng. Mater.* **2024**, *26*, 2400301.

[49] B. V. Basheer, J. J. George, S. Siengchin, J. Parameswaranpillai, *Nano-Struct. Nano-Objects* **2020**, *22*, 100429.

[50] G. Mittal, V. Dhand, K. Y. Rhee, S.-J. Park, W. R. Lee, *J. Ind. Eng. Chem.* **2015**, *21*, 11.

[51] F. V. Ferreira, L. D. S. Cividanes, F. S. Brito, B. R. C. de Menezes, W. Franceschi, E. A. N. Simonetti, G. P. Thim, *Functionalizing Graphene and Carbon Nanotubes*, Springer, Cham **2016**, https://doi.org/10.1007/978-3-319-35110-0_2.

[52] M. Kök, M. E. Pekdemir, E. Özen Öner, M. Coşkun, S. Hekim, *J. Mol. Struct.* **2023**, *1279*, 134989.

[53] S. A. Pineda-Castillo, J. Luo, H. Lee, B. N. Bohnstedt, Y. Liu, C.-H. Lee, *Adv. Eng. Mater.* **2021**, *23*, 2100322.

[54] C. M. B. Ho, A. Mishra, P. T. P. Lin, S. H. Ng, W. Y. Yeong, Y. Kim, Y. Yoon, *Macromol. Biosci.* **2017**, *17*, 1600250.

[55] M. Rahmandoust, M. R. Ayatollahi, **2016**, pp. 5–63.

[56] E. T. Thostenson, Z. Ren, T.-W. Chou, *Compos. Sci. Technol.* **2001**, *61*, 1899.

[57] A. K.-T. Lau, D. Hui, *Compos. Part B Eng.* **2002**, *33*, 263.

[58] M. H. Al-Saleh, U. Sundararaj, *Carbon* **2009**, *47*, 1738.

[59] E. Pop, D. Mann, Q. Wang, K. Goodson, H. Dai, *Nano Lett.* **2006**, *6*, 96.

[60] E. Thostenson, C. Li, T. Chou, *Compos. Sci. Technol.* **2005**, *65*, 491.

[61] T. W. Ebbesen, H. J. Lezec, H. Hiura, J. W. Bennett, H. F. Ghaemi, T. Thio, *Nature* **1996**, *382*, 54.

[62] R. Islam Rubel, M. Hasan Ali, M. Abu Jafor, M. Mahmodul Alam, *AIMS Mater. Sci.* **2019**, *6*, 756.

[63] S. Deng, Z. Lin, B. Xu, H. Lin, C. Du, *Polym. Plast. Technol. Eng.* **2015**, *54*, 1017.

[64] M. V. Kharlamova, M. Paukov, M. G. Burdanova, *Materials* **2022**, *15*, 5386.

[65] K. Shimizu, A. Uchiyama, M. Yamashita, A. Hirose, T. Nishimura, N. Oku, *J. Toxicol. Sci.* **2013**, *38*, 7.

[66] L. A. Lara-Martínez, F. Massó, E. P. González, I. García-Peláez, A. Contreras–Ramos, M. Valverde, E. Rojas, F. Cervantes-Sodi, S. Hernández-Gutiérrez, *Int. J. Nanomed.* **2017**, *12*, 7695.

[67] M. Bottini, N. Rosato, N. Bottini, *Biomacromolecules* **2011**, *12*, 3381.

[68] N. Tsubokawa, *Polym. J.* **2005**, *37*, 637.

[69] X. Zhang, C. Fu, L. Feng, Y. Ji, L. Tao, Q. Huang, S. Li, Y. Wei, *Polymer* **2012**, *53*, 3178.

[70] D. Tasis, N. Tagmatarchis, A. Bianco, M. Prato, *Chem. Rev.* **2006**, *106*, 1105.

[71] F. Avilés, J. V. Cauich-Rodríguez, L. Moo-Tah, A. May-Pat, R. Vargas-Coronado, *Carbon* **2009**, *47*, 2970.

[72] A. Mamun, V. H. Mareau, J. Chen, R. E. Prud'homme, *Polymer* **2014**, *55*, 2179.

[73] D. Rahmatabadi, M. Khajepour, A. Bayati, K. Mirasadi, M. Amin Yousefi, A. Shegeft, I. Ghasemi, M. Baniassadi, K. Abrinia, M. Bodaghi, M. Baghani, *Eur. Polym. J.* **2024**, *216*, 113289.

[74] D. Rahmatabadi, I. Ghasemi, M. Baniassadi, K. Abrinia, M. Baghani, *J. Mater. Res. Technol.* **2022**, *21*, 3970.

[75] A. J. Kinloch, S. J. Shaw, D. A. Tod, D. L. Hunston, *Polymer* **1983**, *24*, 1341.

[76] J. Ghorbani, P. Koirala, Y.-L. Shen, M. Tehrani, *J. Manuf. Process.* **2022**, *80*, 651.

[77] J. E. Seppala, S. Hoon Han, K. E. Hillgartner, C. S. Davis, K. B. Migler, *Soft Matter* **2017**, *13*, 6761.

[78] Y. Tao, F. Kong, Z. Li, J. Zhang, X. Zhao, Q. Yin, D. Xing, P. Li, *A Review on Voids Of 3D Printed Parts By Fused Filament Fabrication*, Vol. *15*, Elsevier, Amsterdam **2021**, pp. 4860–4879.

[79] S. Liu, X. Dong, Y. Wang, J. Xiong, R. Guo, J. Xiao, C. Sun, F. Zhai, X. Wang, *Adv. Mater. Technol.* **2023**, *8*, 1.

[80] Y. Mohseni, M. Mohseni, S. Suresh, M. Riotto, A. Jaggessar, J. P. Little, M.-L. Wille, P. K. Yarlagadda, *Mater. Today Proc.* **2023**.

[81] L. M. Robeson, *J. Vinyl Technol.* **1990**, *12*, 89.

[82] R. E. Prud'homme, *Polym. Eng. Sci.* **1982**, *22*, 90.

[83] M. Ehteramian, I. Ghasemi, H. Azizi, M. Karrabi, *Iran. Polym. J.* **2021**, *30*, 411.

[84] S. Kim, V. F. Korolovych, R. L. Muhlbauer, V. V. Tsukruk, *J. Appl. Polym. Sci.* **2020**, *137*, 49381.

[85] X. Zhang, L. Chen, *Polym. Test.* November **2020**, *91*, 106785.

[86] N. Dhakal, X. Wang, C. Espejo, A. Morina, N. Emami, *J. Mater. Res. Technol.* March–April **2023**, *23*, 1252.

[87] K. Mirasadi, D. Rahmatabadi, I. Ghasemi, M. Khodaei, M. Baniassadi, M. Baghani, *Macromol. Mater. Eng.* **2024**, *309*, 2400038.

[88] W. T. Nugroho, Y. Dong, A. Pramanik, J. Leng, S. Ramakrishna, *Compos. Part B Eng.* **2021**, *223*, 109104.

[89] T. Cheng, M. Thielen, S. Poppinga, Y. Tahouni, D. Wood, T. Steinberg, A. Menges, T. Speck, *Adv. Sci.* **2021**, *8*, 1.

[90] K. Chen, L. Zhang, X. Kuang, V. Li, M. Lei, G. Kang, Z. L. Wang, H. J. Qi, *Adv. Funct. Mater.* **2019**, *29*, 1903568.

[91] T. R. Nachtigall, O. Tomico, R. Wakkary, S. Wensveen, P. van Dongen, L. T. van Noorden, in *Extended Abstracts of the 2018 CHI Conf. Human Factors in Computing Systems*, ACM, New York **2018**, pp. 1–9.

[92] D. C. Ferrier, K. C. Honeychurch, *Biosensors* **2021**, *11*, 486.

[93] L. Joharji, F. Alam, N. El-Atab, *ACS Omega* **2024**, *9*, 14638.

[94] A. Palacios, L. Chiriatti, S. Poppinga, T. Speck, V. Le Houérou, *Adv. Intell. Syst.* **2024**, *7*, 2400396.